ARTICLE

Rapid termination of the African Humid Period triggered by northern high-latitude cooling

James A. Collins [1,2,3], Matthias Prange[3], Thibaut Caley[4], Luis Gimeno[5], Britta Beckmann[3], Stefan Mulitza[3], Charlotte Skonieczny[6], Didier Roche [7,8] & Enno Schefuß[3]

The rapidity and synchrony of the African Humid Period (AHP) termination at around 5.5 ka are debated, and it is unclear what caused a rapid hydroclimate response. Here we analysed the hydrogen isotopic composition of sedimentary leaf-waxes (δD_{wax}) from the Gulf of Guinea, a proxy for regional precipitation in Cameroon and the central Sahel-Sahara. Our record indicates high precipitation during the AHP followed by a rapid decrease at 5.8–4.8 ka. The similarity with a δD_{wax} record from northern East Africa suggests a large-scale atmospheric mechanism. We show that northern high- and mid-latitude cooling weakened the Tropical Easterly Jet and, through feedbacks, strengthened the African Easterly Jet. The associated decrease in precipitation triggered the AHP termination and combined with biogeophysical feedbacks to result in aridification. Our findings suggest that extratropical temperature changes, albeit smaller than during the glacial and deglacial, were important in triggering rapid African aridification during the Holocene.

[1] GFZ–German Research Center for Geosciences, Section 5.1 Geomorphology, Organic Surface Geochemistry Lab, D-14473 Potsdam, Germany. [2] AWI-Alfred Wegener Institute Helmholtz Centre for Polar and Marine Research, Am Alten Hafen 26, D-27568 Bremerhaven, Germany. [3] MARUM—Center for Marine Environmental Sciences, University of Bremen, D-28359 Bremen, Germany. [4] EPOC, CNRS, University of Bordeaux, Allée Geoffroy Saint-Hilaire, 33615 Pessac Cedex, France. [5] Environmental Physics Laboratory (EPhysLab), Facultade de Ciencias, Universidad de Vigo, 32004 Ourense, Spain. [6] Laboratoire GEOsciences Paris-Sud (GEOPS), UMR CNRS 8148, Université de Paris-Sud, Université Paris-Saclay, 91405 Orsay Cedex, France. [7] Faculty of Earth and Life Sciences, Earth and Climate Cluster, Vrije Universiteit Amsterdam, De Boelelaan 1085, 1081 HV Amsterdam, The Netherlands. [8] Laboratoire des Sciences du Climat et de l'Environnement (LSCE), CEA/CNRS-INSU/UVSQ, 91191 Gif-sur-Yvette Cedex, France. Correspondence and requests for materials should be addressed to J.A.C. (email: jcollins@gfz-potsdam.de)

A wide range of studies (e.g., refs. [1, 2]) have shown that most of tropical Africa north of about 10° S was drier during the Last Glacial Maximum (LGM; 23–19 ka), relative to today, and wetter during the early to mid Holocene, which has been defined[3, 4] as the African Humid Period (AHP; ca. 11.5–5.5 ka). Abrupt precipitation changes during the glacial and deglacial are associated with major changes in the Atlantic Meridional Overturning Circulation (AMOC) and sea surface temperature patterns[2, 5]. However, a large and abrupt aridification, with respect to gradual precessional insolation forcing, has also been documented at some sites during the Holocene at ~5.5 ka (the AHP termination)[3, 4], the causes of which are currently unresolved. An abrupt AHP termination was originally thought to have been caused by a collapse of Saharan and Sahelian vegetation at 5.5 ka[6] switching the climate to an arid equilibrium state. Many vegetation records, however, do not show a collapse[4, 7] and the latest coupled climate models[8] suggest the positive biogeophysical feedback was not strong enough to have triggered an abrupt climate switch. Complicating the picture, many hydrological records suggest a gradual (e.g., ref. [7]) or time-transgressive[9, 10] aridification at the AHP termination, more in line with a direct and linear response to precessional insolation forcing. Moreover, some intermediate complexity model simulations (e.g., ref. [11]) have difficulty in simulating an abrupt AHP response and most fully coupled models underestimate the intensity of precipitation during the AHP[9, 12]. Overall, it is not resolved whether a rapid termination of the AHP was ubiquitous and synchronous at 5.5 ka, why this took place at 5.5 ka, and whether additional feedbacks or teleconnections were involved.

Precipitation in tropical Africa results from a combination of factors including the monsoonal on-land flow of moist air, low-level convergence of air at the intertropical convergence zone and, of particular importance, the deep vertical motion of air, which over northern Africa is modulated by the interaction of the Tropical Easterly Jet (TEJ) and the African Easterly Jet (AEJ)[13]. These jets oscillate seasonally and at present reach maximum latitudes of 6–8° N (TEJ) and 14–17° N (AEJ) in August[13]. The TEJ maximum wind-speed is in the upper troposphere at ~150 hPa, while the AEJ maximum windspeed is in the mid-troposphere at ~600 hPa. The TEJ extends from India across the African continent (Fig. 1a, Supplementary Fig. 1) and is maintained by the upper tropospheric temperature gradient between the equatorial latitudes and the relatively
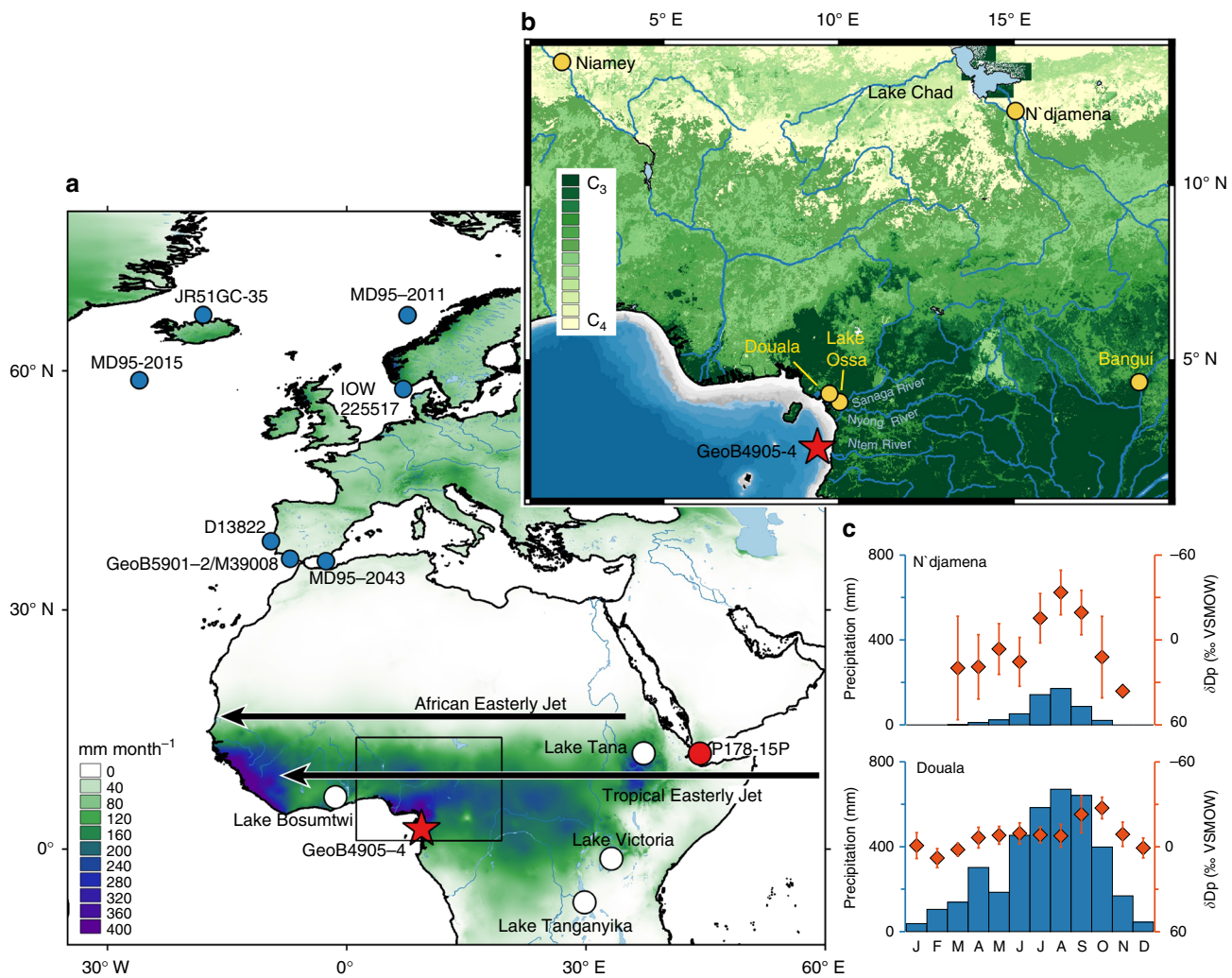

Fig. 1 Maps of the study area and climatology. **a** Colours represent mean monthly precipitation (mm) for the months Jun to Oct, the primary wet seasons for southern Cameroon and the Sahel. Red star marks the study site GeoB4905-4 (2°30.0´ N, 09°23.4´ E) in the Gulf of Guinea. Red dot marks the Gulf of Aden P178-15P core site[4], white dots mark other sites discussed in the text and blue dots mark SST records from Supplementary Table 1. Black arrows mark position of TEJ and AEJ in summer[13]. Black box marks the inset. **b** Zoomed-in map of the study region showing C₃–C₄ vegetation distribution, rivers and bathymetry. Yellow dots mark the Douala, N'djamena, Niamey and Bangui GNIP stations, and Lake Ossa. Bathymetry shallower than 120 m is coloured in grey. **c** Monthly precipitation amount and δDp data for N'djamena, Chad and Doula, Cameroon[27], highlighting the large seasonal δDp changes in the Sahel compared to equatorial regions. Error bars represent standard deviation (1σ) of monthly measurements

warmer subtropics[14]. A slower TEJ is associated with drier conditions in these regions, due to reduced upper-level divergence and hence reduced upward vertical flow[13, 15, 16]. The AEJ is attributed to the meridional temperature gradient in the Sahel and a faster AEJ results in greater moisture export and drier conditions in the western Sahel[13, 17]. The African rainbelt oscillates across southern Cameroon twice a year, bringing most precipitation during northern hemisphere autumn (Sep–Oct–Nov; SON) and some during spring (Mar–Apr–May; MAM), while northern Cameroon and the Sahel receive precipitation primarily during summer (Jun–Jul–Aug; JJA; Fig. 1a).

Sedimentary leaf-wax n-alkane δD (δD_{wax}) has been shown to primarily reflect precipitation δD (δD_{p}) in Cameroon and globally, and in the tropics is often taken to reflect precipitation amount[18]. While biosynthesis of leaf-wax n-alkanes is thought to exert a constant hydrogen isotope fractionation against leaf water, secondary controls on δD_{wax} include relative humidity and vegetation type[13]. δD_{wax} from C_4 grasses is less sensitive to transpirational D enrichment in plant leaves, likely due to partial use of unenriched xylem water in n-alkane synthesis[19]. Other plant physiological differences such as the water source available to the plant and seasonal timing of leaf-wax biosynthesis may also influence δD_{wax} values[18]. Higher relative humidity is thought to reduce evapotranspirational isotopic enrichment of leaf and soil waters, so that in the tropics relative humidity variability tends to amplify the δD_{wax} variability that is driven by the amount effect[18].

Sedimentary $\delta^{13}C_{wax}$ is often used as an indicator of C_3 and C_4 vegetation-type changes. African C_3 trees, shrubs, herbs and lianas

($n = 45$) exhibit a mean (C_{29} n-alkane) $\delta^{13}C_{wax}$ value of $-35.7‰ \pm 2.9‰$[20] while African C_4 grasses ($n = 38$) exhibit a mean $\delta^{13}C_{wax}$ value of $-21.4‰ \pm 2.0‰$[21]. Much of the catchments of the Ntem, Nyong and Sanaga Rivers are dominated by C_3 trees (Fig. 1b)[22] and this is reflected in surface sediments of Lake Ossa, southern Cameroon (Fig. 1b), which exhibit a $\delta^{13}C_{wax}$ value of $-35.4‰$[23]. Conversely, further north, the Sahel-Sahara and much of the Niger River catchment are dominated by C_4 plants (Fig. 1b)[22], and this is evident in marine sediments off West Africa[24].

To provide more insights into the AHP termination, we assess large-scale hydroclimatic changes in Cameroon and the central Sahel-Sahara using δD_{wax} from a marine sediment core GeoB4905-4 in the Gulf of Guinea (Figs. 1a, b). We also assessed $\delta^{13}C_{wax}$ as an indicator for C_3 vs. C_4 vegetation type. Our results indicate high precipitation during the AHP followed by a rapid precipitation decrease at 5.8-4.8 ka, similar to a record from northern East Africa[4]. We show that the rapid precipitation decrease was likely triggered by northern high-latitude cooling. The cooling reduced the speed of the TEJ, triggering rainfall reduction that was amplified by climate feedbacks and resulted in strong aridification over a relatively short period.

Results

Moisture sources. To assess the likely moisture sources to present-day southern Cameroon, we performed analyses using the 3-D Lagrangian model FLEXPART[25]. The backward airmass trajectories (Fig. 2a–d) indicate the southeast Atlantic and central
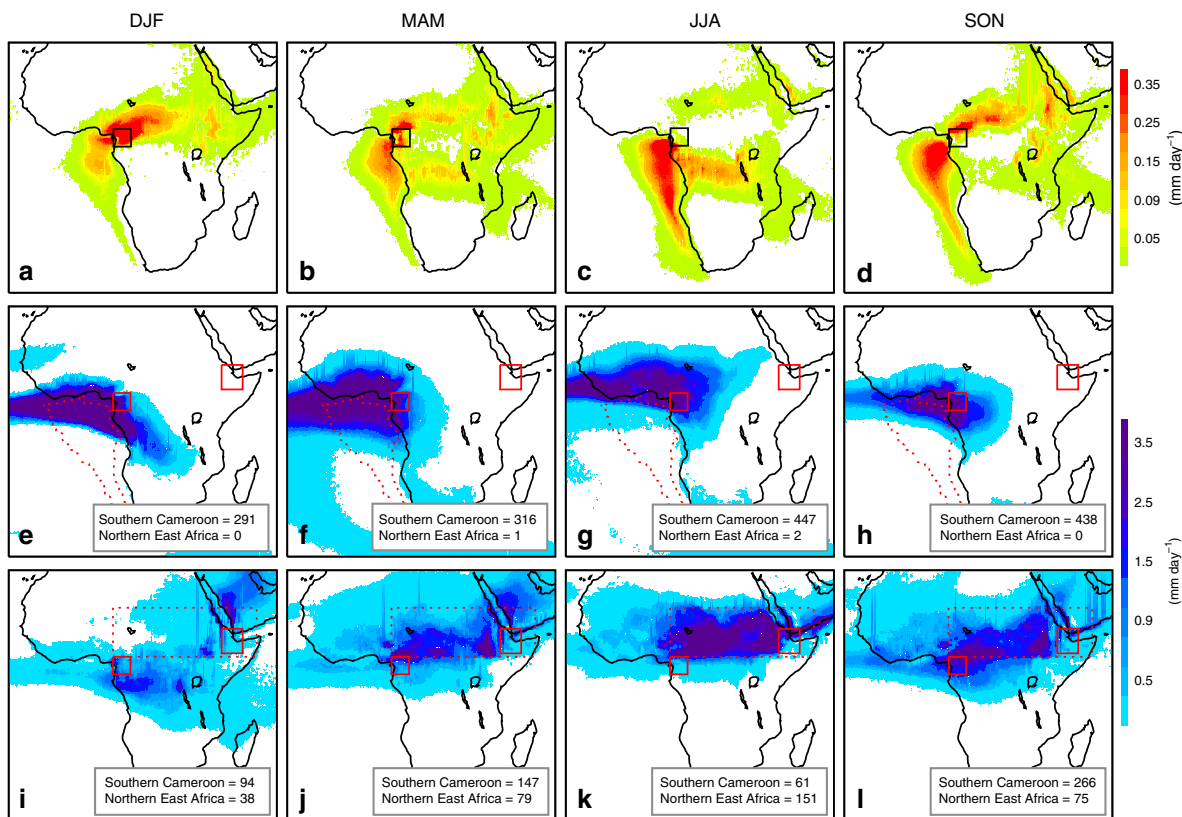

Fig. 2 Moisture sources for southern Cameroon and northern East Africa. **a–d** FLEXPART[84, 85] backward analyses of air mass trajectory for the period 1980–2015 at 0.25° resolution. The boxed region in southern Cameroon (9° E-14° E and 1° N-6° N) represents the estimated leaf-wax source region for Gulf of Guinea core GeoB4905-4. Colours represent the sources of moisture for the boxed region and show where E-P > 0 (mm day^{-1}). **e–h** Forward runs of FLEXPART for the southeast Atlantic moisture source (outlined with a red dashed line). Colours show precipitation derived from this moisture source (mm day^{-1}). Numbers indicate total seasonal precipitation amount (mm) from this moisture-source delivered to the boxed regions in southern Cameroon and northern East Africa. The boxed region in northern East Africa represents the leaf-wax source region for the Gulf of Aden core P178-15P, estimated as 40° E-46° E and 7° N-14° N. **i–l** As **e–h** but for the Sahel-Sahara moisture source (9° E-50° E and 6° N-20° N; marked with a red dashed rectangle). **a, e, i** represent Dec-Jan-Feb (DJF), **b, f, j** represent Mar-Apr-May (MAM), **c, g, k** represent Jun-Jul-Aug (JJA) and **d, h, l** represent Sep-Oct-Nov (SON)
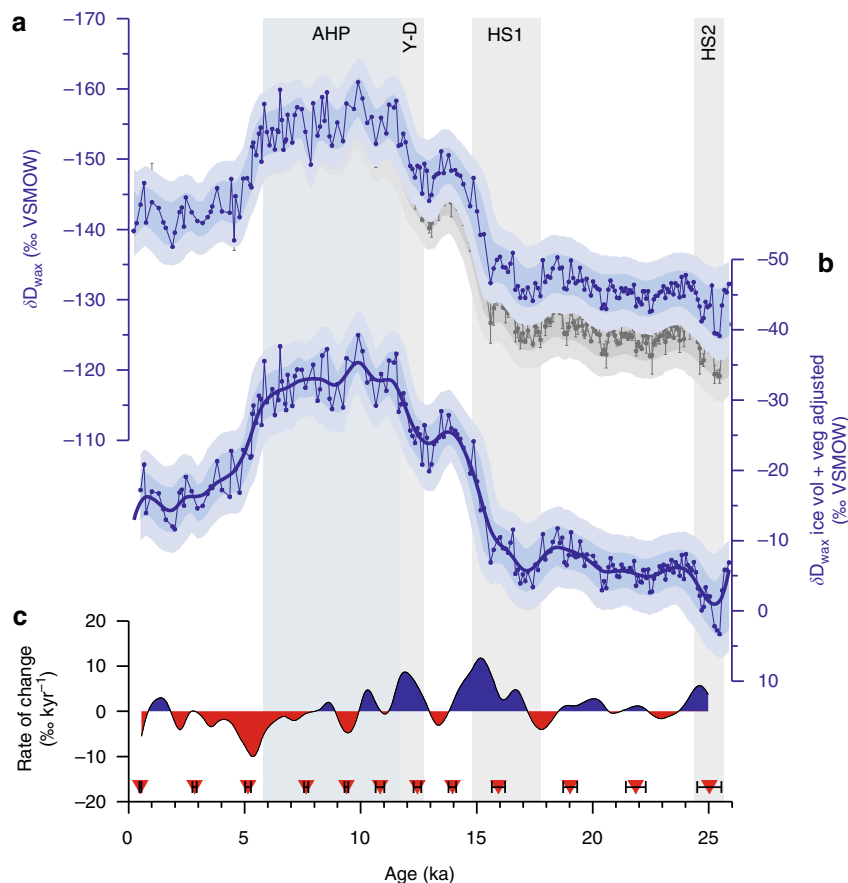
Fig. 3 δD_{wax} from core GeoB4905-4 in the Gulf of Guinea. **a** Grey timeseries represents unadjusted δD_{wax}. Error bars are individual analytical uncertainty. Shadings indicate 68 and 95% uncertainty bounds, including a mean analytical uncertainty of 3‰ and age uncertainty. Blue timeseries represents δD_{wax} adjusted for ice volume, shading as above. **b** δD_{wax} adjusted for ice-volume and vegetation-type changes, representing an estimate of past δD_p. Shadings as above. Thick black line is the Ruppert-Sheather-Wand smooth, the optimal smoothing for the data set[86]. **c** Rate of change (‰ kyr⁻¹) based on Ruppert-Sheather-Wand smooth. Blue colours representing periods of wettening, red represent periods of aridification. Red diamonds mark calibrated radiocarbon age control points. Vertical bars highlight the African Humid Period (AHP), Younger-Dryas (Y-D) and Heinrich Stadials 1 and 2 (HS1, HS2)

Sahel-Sahara to be the major moisture sources to southern Cameroon during the SON and MAM seasons. Forward analyses for the southeast Atlantic (Fig. 2e–h) and Sahel-Sahara (Fig. 2i–l) moisture sources reveal the spatial distribution and amount of precipitation that is generated by the moisture derived from these two sources. This shows that the southeast Atlantic and Sahel-Sahara moisture sources contribute 438 mm and 266 mm of precipitation to southern Cameroon, respectively, for SON season, and 1492 mm and 568 mm over the year.

δD_{wax} and $\delta^{13}C_{wax}$ variability. We focus on the C_{29} *n*-alkane, denoted as δD_{wax} and $\delta^{13}C_{wax}$ (Supplementary Notes 1 and 2). The $\delta^{13}C_{wax}$ values from GeoB4905-4 are generally low and display small variability, ranging between −33.5‰ and −30.3‰ (Supplementary Fig. 2). δD_{wax} values have been adjusted for the effect of ice-volume and vegetation-type changes (Methods section; Fig. 3a, b), although this has a minor effect on the climate signal. The adjusted δD_{wax} record (Fig. 3b) displays large variability and three main transitions. δD_{wax} values were higher during the LGM (23–19 ka) relative to today. As indicated by SiZer analysis (Methods section; Fig. 4), this is followed by two periods of significant δD_{wax} decrease: between 15.9 and 13.9 ka (the end of Heinrich Stadial 1; HS1) and between 12.5 and 11.5 ka (the end of the Younger-Dryas; Y-D). The mean rates of change for these two transition periods are 8‰ kyr⁻¹ and 7‰

kyr⁻¹, respectively (Fig. 3c). δD_{wax} values remained low between 11.5 and 5.8 ka, corresponding to the AHP. Between 5.8 ka and 4.8 ka the record shows a significant δD_{wax} increase (Figs. 3b, c and 4), associated with the AHP termination. In particular, there is a significant increase at lower bandwidths at 5.3 ka, indicating a particularly rapid drying at this time (Fig. 4). The mean rate of change during the AHP termination (5.8 ka and 4.8 ka) is 8‰ kyr⁻¹.

Origin of the δD_{wax} signal. Relatively low $\delta^{13}C_{wax}$ values (mean of −32.3‰, range from −33.5‰ to −30.3‰; Supplementary Fig. 2) over the past 25 kyr suggest that leaf waxes were mainly derived from C_3 vegetation. This agrees with previous work[26] that the catchments of the Ntem, Nyong and Sanaga Rivers were the main source region of leaf-wax *n*-alkanes to the core site (Supplementary Note 2). Nonetheless, our data indicates a slightly higher C_4 contribution than Lake Ossa surface sediment (−35.4‰; ref. [23]) especially during the late Holocene. This points to an additional C_4 contribution to the marine sediment that was probably delivered to the core site as Sahelian-Saharan dust (from, for example, the Bodélé depression) and/or Niger River material. Based on linear mixing with the above C_3 and C_4 end-members, $\delta^{13}C_{wax}$ values over the last 25 kyr would correspond to mean a C_4 vegetation contribution of 24%, with a range between 15 and 41%.
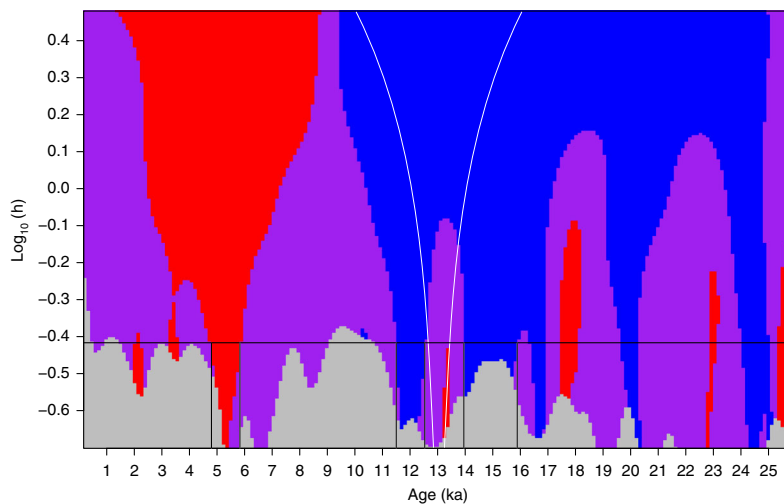
Fig. 4 SiZer map for GeoB4905-4 δD_{wax}. The *y*-axis represents the range of bandwidths (*h*) for which the data were smoothed (plotted on a log scale) and the *x*-axis represents age. Blue regions represent significant decreases in δD_{wax} (wettening), red regions significant increases in δD_{wax} (drying), purple regions no significant change, and grey areas indicate where the sampling resolution is too low. The black horizontal line represents the data-driven Ruppert-Sheather-Wand bandwidth[86], the optimal smoothing (global bandwidth) for the entire data set. Time intervals where this line intersects with areas of significant increase or decrease are highlighted with vertical lines. δD_{wax} is adjusted for ice volume and vegetation type

The minor $\delta^{13}C_{wax}$ variability (Supplementary Fig. 2) suggests that vegetation type is unlikely to be the main control on δD_{wax}, particularly for the large magnitude change between 5.8 and 4.8 ka, when $\delta^{13}C_{wax}$ shows little change. Rather than changes in vegetation, the δD_{wax} record reflects changes in δD_p. Tropical δD_{wax} records are commonly interpreted as being controlled by the amount effect (e.g. ref. [4]) with higher δD_{wax} values representing drier conditions. Given that most leaf waxes originate from southern Cameroon with a smaller contribution from the Sahel, they likely reflect mainly southern Cameroon δD_p and partly Sahel δD_p. However, the amount effect can operate locally and non-locally, i.e., δD_p from southern Cameroon can reflect the amount effect 'upstream' in the moisture-source region (thus integrating over a larger area than that of the leaf-wax source region). Given that annually almost 30% of the moisture in southern Cameroon originates from the central Sahel-Sahara (Fig. 2), it suggests δD_p in southern Cameroon is significantly affected by hydroclimatic processes in the Sahel-Sahara. A further consideration is that the relationship between precipitation amount and δD_p[27] is steeper at sites in the semi-arid regions of the Sahel compared to the equatorial regions (Supplementary Fig. 3), implying past precipitation changes in the Sahel would cause a larger δD_p change than precipitation changes in southern Cameroon, potentially over-printing the southern Cameroon signal. Thus, changes in δD_{wax} likely reflect integrated changes in precipitation amount in both southern Cameroon and the central Sahel-Sahara.

To understand the upstream signal over time, we investigated δD_p over the last 25 ka using a transient simulation of the intermediate complexity isotope-enabled climate model *i*LOVE-CLIM (Methods section). The transient simulation displays a similar evolution of atmospheric δD_p in southern Cameroon and the Sahel-Sahara (Supplementary Note 3), but a different evolution of precipitation amount in the two regions (Supplementary Fig. 4b–e). This suggests that in this model, southern Cameroon δD_p is reflecting an integrated precipitation amount signal from both Cameroon and the central Sahel-Sahara.

Rapid deglacial and Holocene hydrological changes. The Gulf of Guinea δD_{wax} record suggests slightly drier conditions at the LGM compared to the late Holocene (Fig. 3b). Cooler conditions

at the LGM would suggest that the magnitude of aridification at the LGM relative to the late Holocene is likely to be conservative (Methods section). Drier LGM conditions are in line with most other hydroclimate records from northern Africa (e.g., ref. [1]). Increased precipitation at the terminations of HS1 and the Y-D (Fig. 3b) is seen in other records across much of northern Africa north of ~10° S[2]. Both rapid increases are attributed to: CO_2-driven deglacial tropical SST increase and atmospheric warming, increasing the moisture content of the atmosphere and; to AMOC resumption and northern high-latitude SST increase, allowing the rainbelt to penetrate further northwards[2].

A more surprising finding in our Gulf of Guinea δD_{wax} record is the rapid aridification between 5.8 and 4.8 ka with a particularly sharp drop at 5.3 ka (Figs. 3b, c and 4), which exhibits comparable rate of change and duration to changes at the termination of HS1 and the Y-D. Although our δD_{wax} implies a large aridification between 5.8 and 4.8 ka, salinity changes in the Gulf of Guinea, which reflect Ntem, Nyong and Sanaga River discharge in southern Cameroon, display a smaller increase around this time[28]. This would suggest rapid aridification at the AHP termination was more prominent in the Sahel-Sahara than in southern Cameroon.

δD_{wax} records from other regions. The rapid aridification at the AHP termination is similar to that observed between 5.4 ka and 4.5 ka[4] in the Gulf of Aden, northern East Africa (Fig. 5b, c). The transitions are coeval, within the age uncertainty of the records (±0.3 kyr between 5.8 and 4.8 ka for the Gulf of Guinea record; ±0.1 kyr between 5.4 ka and 4.5 ka for the Gulf of Aden). The mean rate of change for the transition period is 5‰ kyr^{-1} for the Gulf of Aden record, comparable to the Gulf of Guinea record. The leaf-wax source region for the Gulf of Aden record mainly receives rainfall during JJA, and also receives a significant contribution of Sahel-Sahara moisture (Fig. 2i–l), suggesting that the rapid AHP termination was a feature spanning the latitudes of the Sahel during the JJA season. Given wetter conditions in the Sahel and Sahara during the mid-Holocene (e.g., refs. [1, 29]), it is plausible that the Sahel-Sahara was a more important moisture source for Cameroon and northern East Africa during the AHP compared to today.
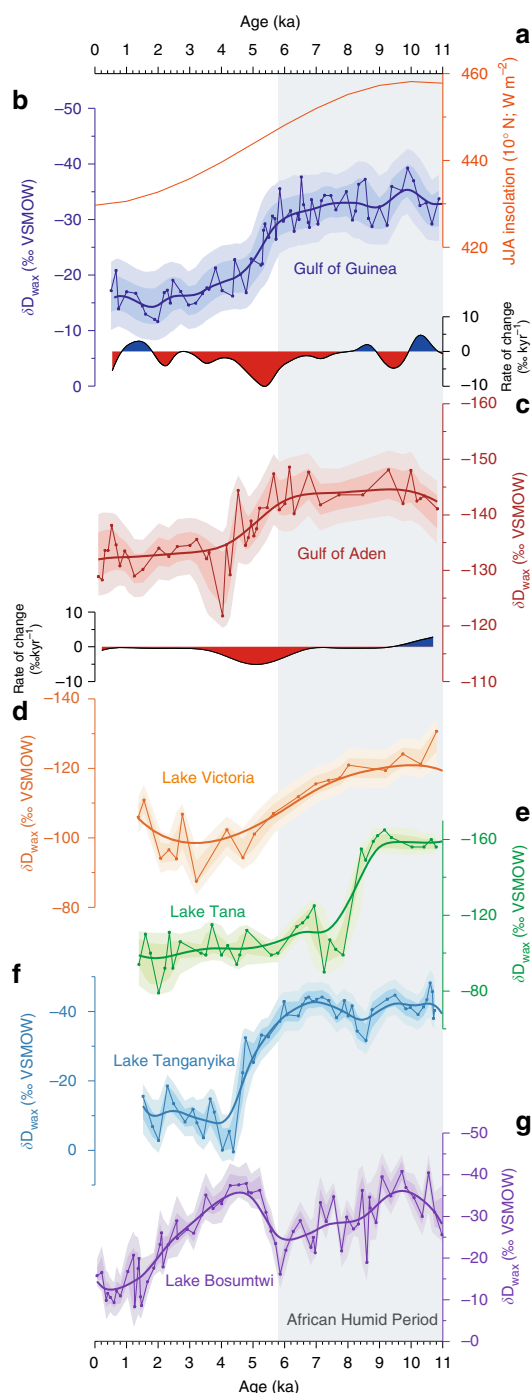
Fig. 5 Comparison with other African δD_{wax} records. **a** Mean JJA insolation at 10° N. **b** Gulf of Guinea δD_{wax} from core GeoB4905-4 (based on the C_{29} n-alkane; ice-volume and vegetation adjusted; this study). **c** Gulf of Aden δD_{wax} (based on the C_{30} fatty acid; ice-volume adjusted) from core P178-15P[4]. **d** Lake Victoria δD_{wax} (based on the C_{28} fatty acid; ice volume adjusted)[30]. **e** Lake Tana δD_{wax} (based on the C_{28} fatty acid; ice volume adjusted)[31]. **f** Lake Tanganyika δD_{wax} (based on the C_{28} fatty acid; ice volume and vegetation adjusted)[33]. **g** Lake Bosumtwi δD_{wax} (based on the C_{31} n-alkane; ice volume and vegetation adjusted)[10]. Shadings indicate 68 and 95% uncertainty bounds, including analytical and age uncertainty. Thick lines represent Ruppert-Sheather-Wand smooth: rate of change (‰ kyr^{-1}) in **b** and **c** is based on this smooth

Other δD_{wax} records from East Africa sometimes show a different evolution at the AHP termination, likely attributable to the seasonality of precipitation and/or moisture-source variability. Lake Victoria displays a relatively gradual δD_{wax} increase from the early to late Holocene (Fig. 5d)[30]: the absence of a rapid change at around 5.5 ka may be because the main wet season at this site is during MAM, and thus δD_p is unlikely to be influenced by Sahel-Sahara JJA moisture. Lake Tana (Fig. 5e) displays a rapid and large magnitude increase at ~8.5 ka, attributed to a reduction in Congo-basin derived recycled moisture[31]. This record displays, however, little δD_{wax} change at 5.5 ka, although sedimentary Ti does show a major decrease at 5.5 ka[32], indicating aridification and perhaps highlighting complex moisture-source effects on δD_{wax} at this site. Lake Tanganyika (Fig. 5f) in eastern Central Africa displays a large and rapid δD_{wax} increase between 5.7 ka and 4.4 ka[33], in line with our record. Lake Tanganyika is located well south of the Sahel, and receives a minor amount of Sahel-Sahara moisture (Fig. 2i-l). The rapid δD_{wax} increase may reflect local aridification, or, given that Lake Tanganyika is also susceptible to E-W moisture shifts[34], may reflect central African moisture-source changes.

In West Africa, the crater lake Bosumtwi δD_{wax} record[10], was interpreted as reflecting reduced precipitation between ~9 ka and 5.5 ka, followed by a return to wet conditions at 5.5 ka and then termination of the AHP at ~3.5 ka (Fig. 5g). Lake Bosumtwi δD_{wax} disagrees, however, with the Bosumtwi lake-level record, which was 110 m higher than today and overflowing the crater rim between 9 ka and 5.7 ka, followed by a lake-level decrease at some point between 5.7 ka and ca. 2.0 ka[10]. The lake-level decrease is thought to have resulted in input of material from the crater walls, as observed in radiocarbon measurements of the late Holocene[35]. Thus, it seems possible that post-highstand Bosumtwi δD_{wax} may be partly biased by input of pre-aged leaf waxes, which could explain the difference to the GeoB4905-4 δD_{wax} record. Offshore NW Africa, δD_{wax} records have shown wet conditions during the AHP; in particular core GC37 displays aridification at about 5.5 ka[9], similar to our record. This was interpreted as a rapid response at the AHP termination, although bioturbation was thought to be significant in these lower-resolution records, making direct comparisons difficult.

Insights from other hydrological proxies. Other proxies from Africa also sometimes show spatially variable responses at the AHP termination. The vegetation record of Lake Yoa was interpreted as representing a gradual aridification through the Holocene[7]. Persistence of wet conditions in this region after the AHP has, however, been attributed to the Tibesti Mountains acting as a 'water tower'[36]. Compilations of past hydrology spanning the Sahel-Sahara have been interpreted as showing a heterogeneous response, with north-south[10] and east-west[29] differences in the timing of aridification. The compilations are, however, partly based on discontinuous records, that are less well dated compared to marine records, and include a range of different hydrological indicators, which together might explain this heterogeneity. Nonetheless, from our record we cannot rule out that the northernmost Sahara[10] dried earlier than the southern Sahara and Sahel.

In support of our record, several other proxies provide additional evidence for a rapid end to the wet conditions of the AHP in the Sahel-Sahara. The lake-level record of Lake Mega-Chad displays high levels until ~5.2 ka, when the water balance rapidly decreased[36]. In NW Africa, the ODP658C dust record shows a very abrupt increase at 5.5 ka[3], and other dust flux records show increases at around 4.9 ka[37], although we note that dust may not necessarily be directly related to hydrology. In
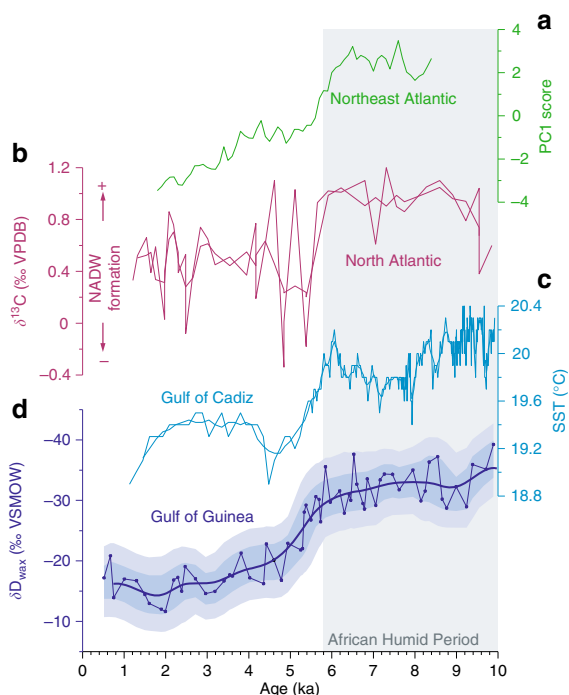
Fig. 6 Comparison with mid- and high-latitude records. **a** Principle Component 1 (PC1) scores from eight alkenone SST records in the northern Atlantic (Supplementary Table 1). PC1 represents 57.8% of the variance. **b** $\delta^{13}C$ of benthic foraminfera from core EN120-GGC1 in the north Atlantic, interpreted as a record of NADW formation and ocean circulation: lower values represent slower ocean circulation[54]. **c** Alkenone SST from core GeoB5901-2 in the Gulf of Cadiz, just to the north of Africa[87]. **d** δD_{wax} from GeoB4905-4 (ice-volume and vegetation adjusted, this study). Shadings indicate 68 and 95% uncertainty bounds, including analytical and age uncertainty

northern East Africa a large increase in the deposition of K-rich sediment, is evident between ~5.8 and 4.8 ka at Chew Bahir[38], indicating aridification, similar to the drop in Ti at 5.5 ka at Lake Tana[32]. Also in northern East Africa, lake levels at Lakes Abhe[39], Zibay Shalla[40] and Abiyata[41] display major decreases at about 4.5 ka, 5.0 ka and 5.4 ka, respectively. Therefore, overall, a number of records lend support to the hypothesis of a rapid AHP termination at about 5.5 ka covering the Sahel-Sahara and northern East Africa.

The role of biogeophysical feedbacks. Hydroclimate stability in the Sahel-Sahara during the AHP followed by a rapid aridification at 5.8–4.8 ka would not be in line with a response to local precessional insolation forcing, which began to decrease at around 9 ka (Fig. 5a). This raises the question of why climate remained wet until 5.8 ka and what caused the large-scale response at this time. Either internal climate feedbacks created a non-linear response to the external forcing due to a threshold in the system, or there was a teleconnection driving the rapid aridification beginning at 5.8 ka.

Sahel-Sahara vegetation and soil moisture are thought to exert a positive feedback effect, i.e., enhancing wetter conditions during the AHP[8]. However, these feedbacks are considered too weak to have caused a tipping point[8], and thus would not themselves have been the initial trigger for the onset of aridification at 5.8 ka. Nonetheless, we do not rule out that these positive feedbacks enhanced the rate of aridification at the AHP termination once underway. Atmospheric dust is also believed to have been an important feedback in enhancing the wetness during the AHP[42],

and thus was potentially another factor enhancing aridification at the AHP termination.

Models indicate that lakes and wetlands may also constitute a positive feedback[43] via modulation of the regional moisture balance. The rapid 100 m depth decrease of Lake Mega-Chad at about 5.2 ka[36] would have reduced the lake area from the maximum estimated extent of 350,000 km^2[44] towards the 'pre-industrial' [1960] value of 25,000 km^2, perhaps reducing moisture contribution and enhancing the rapidity of AHP termination. Nonetheless, other studies suggest that the positive feedback from Lake Chad was weak due to the cool lake surface inhibiting deep convective precipitation[45] and thus it also seems unlikely that lakes and wetlands were the sole trigger for the AHP termination.

An additional potential mechanism invokes tropical SST[4]. It was suggested that Indian Ocean SST decreased below a critical threshold at ~5.0 ka, substantially reducing tropical East African precipitation. However, SST records from both the western Indian Ocean (Supplementary Fig. 5a–c) and Gulf of Guinea (Supplementary Fig. 5d) do not show a significant SST change at this time, suggesting that tropical SSTs were not the trigger for the rapid precipitation decrease on the eastern or western sides of the continent.

Overall, models suggest that vegetation, soil moisture, dust, lake and wetland feedbacks, were not the critical trigger tipping the climate towards a drying state. It is possible that the models are simply deficient in representing these processes. Alternatively, it is possible that a trigger was needed from further afield within the climate system, to initiate the onset of feedbacks and the AHP termination. Because we see rapid aridification on the east and west sides of Africa (Fig. 5b,c), this trigger was likely teleconnected to a large-scale atmospheric circulation feature, such as the TEJ. We suggest that a TEJ slowdown was triggered by a cooling of the Northern Hemisphere mid- and high-latitudes.

High-latitude cooling triggered the AHP termination. A range of records from the northern high latitudes including Greenland[46], the Norwegian sea[47, 48] and the Fram Strait[49, 50] indicate a rapid drop in summer temperature between ~6.0 and 5.0 ka. Other records also indicate an increase in Arctic sea ice[50, 51] at about 5.5 ka. Empirical Orthogonal Function (EOF) analysis of temperature records from Canada and Greenland suggests an onset of rapid cooling at ~5.0 ka[52]. We performed EOF analysis of Holocene alkenone SST records from the Arctic and northeast Atlantic (Supplementary Table 1, Fig. 1a). Although the overall trend of the Principle Component 1 from the analysis is one of gradual insolation driven cooling, it does indicate more rapid cooling between about 6.0 and 5.5 ka than earlier or later in the Holocene (Fig. 6a). Rapid north Atlantic cooling at this time may have been related to an AMOC slowdown between ~6.0 and 5.0 ka[53–55] (Fig. 6b). High-latitude cooling may also have been linked to increased Arctic sea-ice generation, that has been attributed to sea-level induced flooding of the Laptev Sea shelf at ~5.0 ka[49, 56]. Other studies suggested that between 6.0 and 5.0 ka an expanded polar vortex[57] brought winter-like conditions to the mid-latitudes, evident in north America[58]. Cooling is evident in Europe[59] and SSTs just to the north of Africa (Fig. 6c), suggesting that the cool anomaly expanded from the mid-high latitudes towards northern Africa with eastern boundary currents.

To investigate how such a northern extratropical cooling affected African hydrology, we used a high-resolution version of the fully coupled CCSM3 climate model (Methods section). We simulated AHP conditions with an early Holocene (EH, 8.5 ka) control run, and subsequently initiated an extratropical North Atlantic cooling by a freshwater-induced slowdown of the AMOC (experiment EH$_{fre}$). Note that a freshwater perturbation is a
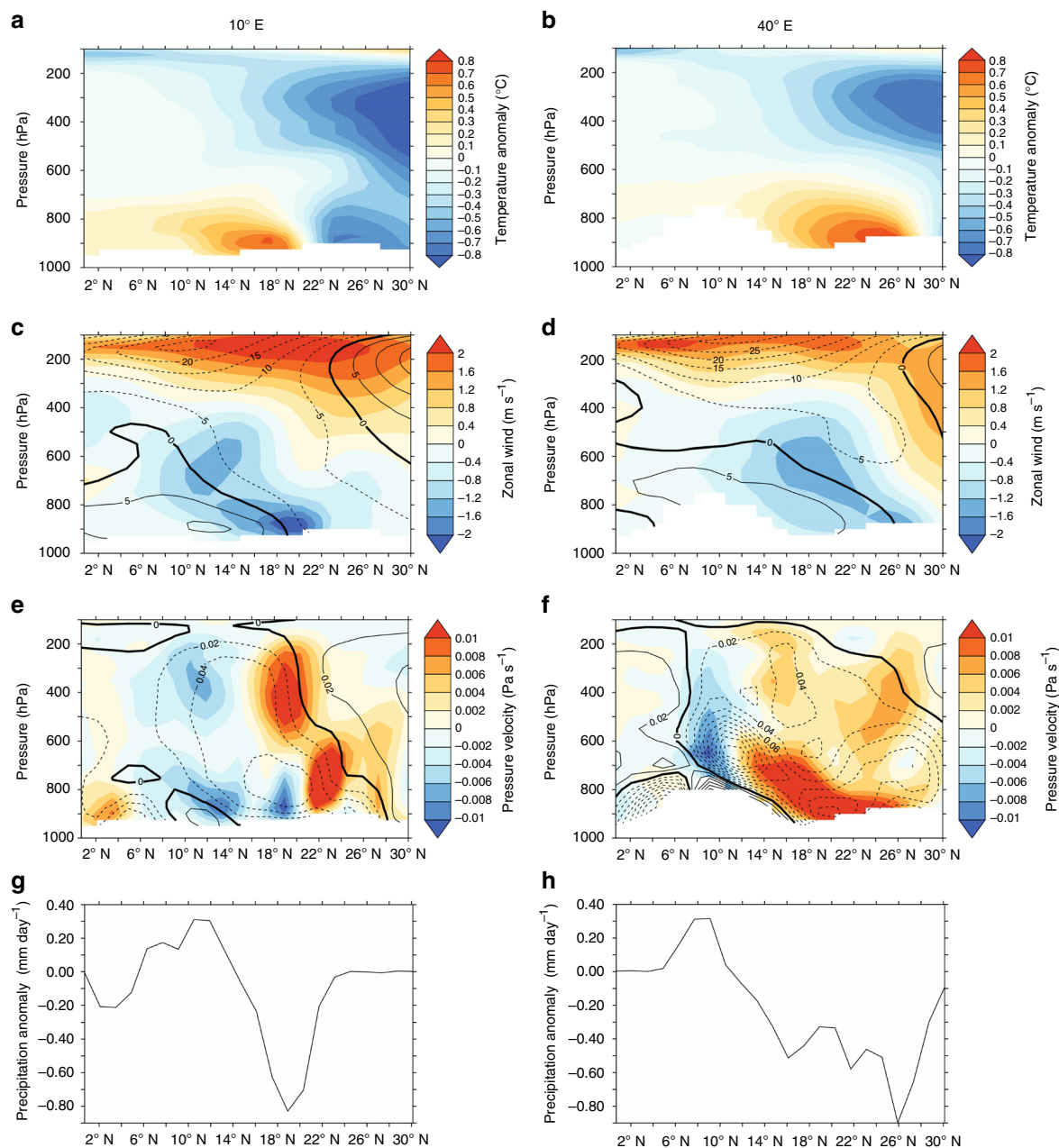
Fig. 7 CCSM3 model output showing the effect of north Atlantic cooling on northern African winds and precipitation during the AHP. Height-latitude plots along longitudes 10° E (**a**, **c**, **e**, **g**) and 40° E (**b**, **d**, **f**, **h**) during JJA season. **a**, **b** Tropospheric temperature anomalies (°C) for the EH$_{fre}$–EH experiment, highlighting the cool anomaly over the northern Sahara. **c**, **d** Zonal wind speed (m s^{-1}), with contours representing the early Holocene control run (EH; negative values represent easterly winds). Shading represents anomalies (EH$_{fre}$—EH): red region around 150 hPa is a negative easterly anomaly, blue region a positive easterly anomaly. **e**, **f** Vertical flow (Pa s^{-1}), with contours representing the EH control run (negative values represent upward motion). Shading represents anomalies (EH$_{fre}$—EH): red shows decreased upward motion, blue increased upward motion. **g** Precipitation anomalies (EH$_{fre}$–EH; mm day^{-1}) along 10° E. **h** Precipitation anomalies (EH$_{fre}$–EH; mm day^{-1}) along 40° E

simple and common method to induce a cooling in the high northern latitudes and we do not imply a large input of freshwater at this time. In experiment EH$_{fre}$, surface temperatures decrease by 0.5–2.5 °C in the northeastern North Atlantic compared to EH. The EH simulation clearly shows the TEJ at ~10° N and 150 hPa and the AEJ at ~20° N and 500–600 hPa (contours in Fig. 7c, d). The simulated EH$_{fre}$–EH anomaly shows that the high- and mid-latitude JJA cooling (Fig. 7a, b) reaches northern Africa. The cool anomaly is evident throughout the troposphere in the northern Sahara from the western-to-central (10° E) and eastern (40° E) regions (Fig. 7a, b), acting to reduce the meridional gradient of upper tropospheric temperature

between the Sahara and the equatorial latitudes. In accordance with the thermal wind relation, this weakens the TEJ (red shading in Fig. 7c, d), leading to reduced upper-level divergence. In the western-to-central region (10° E; Fig. 7c) the slowdown of the TEJ is particularly pronounced at its anticyclonic poleward flank, where the upper-level divergence is usually strongest[60]. This reduces upward vertical motions in the mid to upper troposphere at 16–23° N at 10° E and north of 12° N at 40° E (red and orange regions in Fig. 7e, f) driving a reduction in precipitation at similar latitudes of the Sahel-Sahara (Fig. 7g, h). In addition to the upper tropospheric dynamical processes, surface cooling in the Saharan region is associated with a weakening of the Sahara Heat Low[61],

which reduces the westerly inflow and northward penetration of low-level moist monsoon winds (Fig. 7c, d) and hence moisture convergence. Drier conditions are further associated with a reduced low-level moist static energy and hence a more stable atmosphere, hampering deep convection[61, 62]. These mechanisms strongly agree with previous modern-day model experiments and instrumental/re-analysis data[61–63], although in these experiments, the main area of drying was located further south in the Sahel and central Africa[61], as would be expected in a situation when the Sahara is arid. In the model data[63] it was found that the changes in the TEJ and Sahara Low tend to precede the change in precipitation, suggesting them to be a cause of rather than response to the change in Sahel rainfall. Additionally, during aridification, a shift of the soil moisture and meridional surface temperature gradient has been shown to strengthen the AEJ, further reducing rainfall across the west and central Sahel[17, 64]: thus the AEJ may represent an additional feedback contributing to the rapid aridification at 5.8–4.8 ka. Furthermore, models suggest that the high-latitude cooling was enhanced by the African precipitation decrease[65], and this connection may have contributed to a tipping point behaviour of the two regions.

Discussion

In comparison with the high- and mid-latitude temperature decrease at the AHP termination, the increase at the AHP onset was much larger (e.g., ref. [47]), yet the magnitude of African hydrological change was similar (Fig. 3). This might be taken suggest that high- and mid-latitude temperature only played a secondary role in controlling African precipitation compared to local biogeophysical feedbacks. However, other factors including ice sheet retreat and tropical warming likely had an effect on African precipitation at the AHP onset, inhibiting a direct comparison. Nonetheless, it seems likely[8, 42, 43] that vegetation, dust, lake and wetland feedbacks played a role in amplifying the hydroclimatic shifts at the AHP termination.

In summary, our findings suggest that the effect of rapid high- and mid-latitude temperature changes on tropical African hydroclimate was not restricted to the glacial and deglacial, but also played a decisive role in triggering the AHP termination. Teleconnection of high-mid latitude temperatures with the TEJ reduced JJA precipitation in the Sahel-Sahara, tipping the hydrological system towards an arid state. Although the high-latitude temperature changes were relatively small during the Holocene, the associated initial drying was the required trigger for vegetation, soil moisture, dust and lake feedbacks that together resulted in a large and rapid aridification. From these findings, it appears that future changes in high-latitude SST, in particular associated with sea-ice changes, may have strong implications for low-latitude hydroclimate[66].

Methods

Sediment core and age model. Marine sediment core GeoB4905-4 was recovered at 2°30.0′ N, 09°23.4′ E from 1328 m water depth offshore Cameroon[67]. The age model of the core is based on 12 radiocarbon ages[68, 69] that have been re-calibrated using the Marine13 curve with a reservoir age of 0.4 ± 0.1 kyr. The age-depth relationship was constructed using the software BACON 2.2[70] and represents the median of 10,000 iterations (Supplementary Fig. 6). The mean age uncertainty (1σ) over the last 25 ka is ± 0.3 kyr.

n-Alkane extraction and purification. Extraction and purification were performed at MARUM—Center for Marine Environmental Sciences, Bremen. Sediment samples of 10 ml were taken from core GeoB4905-4 with syringes, which yielded up to 9 g of dry sediment. Samples were oven dried at 40 °C, homogenised and squalane internal standard was added before extraction. Organic compounds were extracted with a DIONEX Accelerated Solvent Extractor (ASE 200) at 100 °C and 1000 psi using a 9:1 mixture of dichloromethane to methanol for 5 min, which was repeated three times. The saturated hydrocarbon fraction was obtained by elution of the dried lipid extract with hexane over a silica gel column (mesh size 60)

followed by elution with hexane over $AgNO_3$-coated silica to remove unsaturated hydrocarbons.

Isotopic analyses. Isotopic analyses were performed at MARUM—Center for Marine Environmental Sciences, Bremen. n-Alkane $\delta^{13}C$ analyses were carried out using a ThermoFisher Scientific Trace GC Ultra coupled to a Finnigan MAT 252 isotope ratio monitoring mass spectrometer via a combustion interface operated at 1000 °C. Isotope values were calibrated against external CO_2 reference gas. The squalane internal standard yielded an accuracy of 0.4‰ and a precision of 0.2‰ (n = 371). Samples were run at least in duplicate, with a reproducibility of on average 0.1‰ for the C_{29} n-alkane. δD values of n-alkanes were measured using a ThermoFisher Scientific Trace GC coupled via a pyrolysis reactor operated at 1420 °C to a ThermoFisher MAT 253 isotope ratio mass spectrometer (GC/IR-MS). δD values were calibrated against external H_2 reference gas. The squalane internal standard yielded an accuracy of 1‰ and a precision of 3‰ on average (n = 428). Samples were analysed at least in duplicate, with an average reproducibility of 1‰ for the C_{29} n-alkane. Repeated analysis of an external n-alkane standard between samples yielded a root-mean-squared accuracy of 2‰ and a standard deviation of on average 3‰. The H_3-factor had a mean of 6.00 ± 0.02 and varied between 5.83 and 6.19 throughout analyses.

δD_{wax} adjustments. We adjusted δD_{wax} for ice volume (following e.g., ref. [4]) using a seawater $\delta^{18}O$ curve[71] and converting to δD assuming a Last Glacial Maximum (LGM) increase of 7.2‰ (Fig. 3a). We use 7.2‰ rather than 8‰ because sediment pore water $\delta^{18}O$ and δD measurements[72] suggest that the glacial δD increase has a mean value of 7.2‰. We also adjusted the δD_{wax} record for vegetation changes (e.g., ref. [73]) using published fractionation factors (−123‰ ± 31‰ for C_3 trees, −139‰ ± 27‰ for C_4 grasses; ref. [18]). End-member C_{29} $\delta^{13}C_{wax}$ values used for C_3 and C_4 vegetation were −35.7‰ and −21.4‰, respectively. The large uncertainties reflect different physiology, water source and seasonal timing of synthesis between plant types. This in turn highlights that a vegetation adjustment distinguishing only between C_3 and C_4 may not capture all potential vegetation changes, for example, between the input of shrubs, bushes and forbs that constitute a small fraction of the source areas[74]. Nonetheless, the highly integrated signal in marine sediments likely averages out much of the vegetation-type effect on δD_{wax}, suggesting such an adjustment to be appropriate in this instance. Overall, the vegetation and ice-volume adjusted δD_{wax} record (Fig. 3b) is similar to the unadjusted record (Fig. 3a), highlighting that the adjustments have a minor effect on the climate signal. Although δD_{wax} records are sometimes adjusted for temperature[75], it is difficult to estimate the past relationship between temperature and δD_p. Given that the sea surface temperature record from GeoB4905-4[69] evolved similarly but in antiphase to δD_{wax}, a temperature adjustment would act to enhance the magnitude of past δD_{wax} changes, suggesting the estimated magnitude of past δD_p changes to be conservative.

SiZer analysis. In order to assess the timing and significance of the transitions in our δD_{wax} record, we performed a SiZer (Significant Zero crossings of derivatives) analysis[76]. This creates a family of Gaussian smooths for the data, and for each smooth identifies the time periods during which the derivative is significantly different from zero. To compare the rapidity of the transitions, we calculated the mean rate of change for these identified time periods.

Climate modelling. Investigations of the effect of high-latitude cooling on African hydroclimate were performed with simulations of a high-resolution version of the fully coupled Community Climate System Model version 3 (CCSM3). In this model version, the atmosphere model has a T85 (1.4° transform grid) resolution with 26 levels in the vertical, while the ocean has a nominal 1° horizontal resolution with 25 levels[77]. To study AHP conditions, we analysed a control simulation at 8.5 ka. In this early Holocene (EH) experiment, we used the orbital parameters and greenhouse gas concentrations for 8500 years before present (CO_2 = 260 ppmv, CH_4 = 660 ppbv, N_2O = 260 ppbv)[78]. The EH experiment has been spun up over a period of 1400 years. In order to cool down the northern extratropics, a freshwater hosing was subsequently applied to the EH control run (experiment EH_{fre}), in which freshwater at a rate of 0.2 Sv was injected into the northern North Atlantic for 400 years[79]. From both experiments (control and hosing) the last 100 years were taken and averaged for analyzes.

Investigations of the source of the atmospheric δD_p signal were performed with a transient run of the intermediate complexity isotope-enabled climate model iLOVECLIM[80–82]. We studied the last 25 kyr of a 150 kyr simulation, which was run with the atmosphere at 5.6° resolution and used accelerated forcing (irradiance, GHGs and ice sheets were updated with an acceleration factor 10)[83]. Intermediate complexity models such as this have difficulty reproducing precipitation, but have the advantage of producing a continuous transient simulation of water isotopes for comparison with proxy data.

Code availability. CCSM3 source code is disseminated via the Earth System Grid (www.earthsystemgrid.org). Full model documentation is available at http://www.cesm.ucar.edu/models/ccsm3.0/.

The *iLOVECLIM* source code is based on the LOVECLIM model version 1.2, whose code is accessible at http://www.elic.ucl.ac.be/modx/elic/index.php?id=289. The developments on the *iLOVECLIM* source code are hosted at https://forge.ipsl.jussieu.fr/ludus, but are not publicly available due to copyright restrictions. Access can be granted on demand by request to D. M. Roche (didier.roche@lsce.ipsl.fr) to those who conduct research in collaboration with the *iLOVECLIM* users group.

References

1. Gasse, F. Hydrological changes in the African tropics since the Last Glacial Maximum. *Quat. Sci. Rev.* **19**, 189–211 (2000).
2. Otto-Bliesner, B. L. et al. Coherent changes of southeastern equatorial and northern African rainfall during the last deglaciation. *Science* **346**, 1223–1227 (2014).
3. deMenocal, P. et al. Abrupt onset and termination of the African Humid Period: rapid climate responses to gradual insolation forcing. *Quat. Sci. Rev.* **19**, 347–361 (2000).
4. Tierney, J. E. & deMenocal, P. Abrupt shifts in Horn of Africa hydroclimate since the Last Glacial Maximum. *Science* **342**, 843–846 (2013).
5. Niedermeyer, E. M. et al. Extratropical forcing of Sahel aridity during Heinrich stadials. *Geophys. Res. Lett.* **36**, L20707 (2009).
6. Claussen, M. et al. Simulation of an abrupt change in Saharan vegetation in the Mid-Holocene. *Geophys. Res. Lett.* **26**, 2037–2040 (1999).
7. Kröpelin, S. et al. Climate-driven ecosystem succession in the sahara: the past 6000 years. *Science* **320**, 765–768 (2008).
8. Rachmayani, R., Prange, M. & Schulz, M. North African vegetation–precipitation feedback in early and mid-Holocene climate simulations with CCSM3-DGVM. *Clim. Past* **11**, 175–185 (2015).
9. Tierney, J. E., Pausata, F. S. & deMenocal, P. Rainfall regimes of the Green Sahara. *Sci. Adv.* **3**, e1601503 (2017).
10. Shanahan, T. M. et al. The time-transgressive termination of the African Humid Period. *Nat. Geosci.* **8**, 140–144 (2015).
11. Wang, Y., Mysak, L. A., Wang, Z. & Brovkin, V. The greening of the McGill Paleoclimate Model. Part II: simulation of Holocene millennial-scale natural climate changes. *Clim. Dyn.* **24**, 481–496 (2005).
12. Zheng, W. & Braconnot, P. Characterization of model spread in PMIP2 mid-Holocene simulations of the African monsoon. *J. Clim.* **26**, 1192–1210 (2013).
13. Nicholson, S. E. On the factors modulating the intensity of the tropical rainbelt over West Africa. *Int. J. Climatol.* **29**, 673–689 (2009).
14. Koteswaram, P. The easterly jet stream in the tropics. *Tellus* **10**, 43–57 (1958).
15. Hulme, M. & Tosdevin, N. The tropical easterly jet and Sudan rainfall: a review. *Theor. Appl. Climatol.* **39**, 179–187 (1989).
16. Segele, Z. T., Lamb, P. J. & Leslie, L. M. Large-scale atmospheric circulation and global sea surface temperature associations with Horn of Africa June–September rainfall. *Int. J. Climatol.* **29**, 1075–1100 (2009).
17. Patricola, C. & Cook, K. H. Atmosphere/vegetation feedbacks: a mechanism for abrupt climate change over northern Africa. *J. Geophys. Res. Atmos.* **113**, D18102 (2008).
18. Sachse, D. et al. Molecular paleohydrology: interpreting the hydrogen-isotopic composition of lipid biomarkers from photosynthesizing organisms. *Annu. Rev. Earth Planet. Sci.* **40**, 221–249 (2012).
19. Kahmen, A., Schefuß, E. & Sachse, D. Leaf water deuterium enrichment shapes leaf wax *n*-alkane δD values of angiosperm plants I: experimental evidence and mechanistic insights. *Geochim. Cosmochim. Acta* **111**, 39–49 (2013).
20. Vogts, A., Moossen, H., Rommerskirchen, F. & Rullkötter, J. Distribution patterns and stable carbon isotopic composition of alkanes and alkan-1-ols from plant waxes of African rain forest and savanna C$_3$ species. *Org. Geochem.* **40**, 1037–1054 (2009).
21. Rommerskirchen, F., Plader, A., Eglinton, G., Chikaraishi, Y. & Rullkötter, J. Chemotaxonomic significance of distribution and stable carbon isotopic composition of long-chain alkanes and alkan-1-ols in C$_4$ grass waxes. *Org. Geochem.* **37**, 1303–1332 (2006).
22. Still, C. J. Powell R. L. in *Isoscapes: understanding movement, pattern, and process on Earth through isotope mapping* (eds West, J. B., Bowen, G. J., Dawson, T.E., and Tu, K. P.) (Springer, Dordrecht, 2010).
23. Garcin, Y. et al. Hydrogen isotope ratios of lacustrine sedimentary n-alkanes as proxies of tropical African hydrology: insights from a calibration transect across Cameroon. *Geochim. Cosmochim. Acta* **79**, 106–126 (2012).
24. Collins, J. A. et al. Interhemispheric symmetry of the tropical African rainbelt over the past 23,000 years. *Nat. Geosci.* **4**, 42–45 (2011).
25. Gimeno, L. et al. Oceanic and terrestrial sources of continental precipitation. *Rev. Geophys.* **50**, RG4003 (2012).
26. Weldeab, S., Frank, M., Stichel, T., Haley, B. & Sangen, M. Spatio-temporal evolution of the West African monsoon during the last deglaciation. *Geophys. Res. Lett.* **38**, L13703 (2011).
27. IAEA/WMO, Global Network of Isotopes in Precipitation. The GNIP Database. Accessible at: http://www.iaea.org/water. (2006).
28. Weldeab, S., Lea, D. W., Schneider, R. R. & Andersen, N. 155,000 years of West African monsoon and ocean thermal evolution. *Science* **316**, 1303–1307 (2007).
29. Lézine, A.-M., Hély, C., Grenier, C., Braconnot, P. & Krinner, G. Sahara and Sahel vulnerability to climate changes, lessons from Holocene hydrological data. *Quat. Sci. Rev.* **30**, 3001–3012 (2011).
30. Berke, M. A. et al. Molecular records of climate variability and vegetation response since the Late Pleistocene in the Lake Victoria basin, East Africa. *Quat. Sci. Rev.* **55**, 59–74 (2012).
31. Costa, K., Russell, J., Konecky, B. & Lamb, H. Isotopic reconstruction of the African Humid Period and Congo air boundary migration at Lake Tana, Ethiopia. *Quat. Sci. Rev.* **83**, 58–67 (2014).
32. Marshall, M. H. et al. Late Pleistocene and Holocene drought events at Lake Tana, the source of the Blue Nile. *Global Planet. Change* **78**, 147–161 (2011).
33. Tierney, J. E. et al. Northern hemisphere controls on tropical southeast African climate during the past 60,000 Years. *Science* **322**, 252–255 (2008).
34. Lewis, S. C., LeGrande, A. N., Kelley, M. & Schmidt, G. A. Water vapour source impacts on oxygen isotope variability in tropical precipitation during Heinrich events. *Clim. Past* **6**, 325–343 (2010).
35. Shanahan, T. M. et al. The formation of biogeochemical laminations in Lake Bosumtwi, Ghana, and their usefulness as indicators of past environmental changes. *J. Paleolimnol.* **40**, 339–355 (2008).
36. Armitage, S. J., Bristow, C. S. & Drake, N. A. West African monsoon dynamics inferred from abrupt fluctuations of Lake Mega-Chad. *Proc. Natl Acad. Sci. USA* **112**, 8543–8548 (2015).
37. McGee, D., Winckler, G., Stuut, J. & Bradtmiller, L. The magnitude, timing and abruptness of changes in North African dust deposition over the last 20,000 yr. *Earth Planet. Sci. Lett.* **371**, 163–176 (2013).
38. Foerster, V. et al. Environmental change and human occupation of southern Ethiopia and northern Kenya during the last 20,000 years. *Quat. Sci. Rev.* **129**, 333–340 (2015).
39. Gasse, F. & Van Campo, E. Abrupt post-glacial climate events in West Asia and North Africa monsoon domains. *Earth Planet. Sci. Lett.* **126**, 435–456 (1994).
40. Gillespie, R., Street-Perrott, F. A. & Switsur, R. Post-glacial arid episodes in Ethiopia have implications for climate prediction. *Nature* **306**, 680–683 (1983).
41. Chalié, F. & Gasse, F. Late Glacial–Holocene diatom record of water chemistry and lake level change from the tropical East African Rift Lake Abiyata (Ethiopia). *Palaeogeogr. Palaeoclimatol. Palaeoecol.* **187**, 259–283 (2002).
42. Pausata, F. S. R., Messori, G. & Qiong, Z. Impacts of dust reduction on the northward expansion oftheAfricanmonsoon during the Green Sahara period. *Earth Planet. Sci. Lett.* **434**, 298–307 (2016).
43. G. Krinner et al. A reassessment of lake and wetland feedbacks on the North African Holocene climate. *Geophys. Res. Lett.* **39**, L07701 (2012).
44. Schuster, M. et al. Holocene lake Mega-Chad palaeoshorelines from space. *Quat. Sci. Rev.* **24**, 1821–1827 (2005).
45. Lauwaet, D., Van Lipzig, N., Van Weverberg, K., De Ridder, K. & Goyens, C. The precipitation response to the desiccation of Lake Chad. *Q. J. R. Meteorol. Soc.* **138**, 707–719 (2012).
46. D'Andrea, W. J., Huang, Y., Fritz, S. C. & Anderson, N. J. Abrupt Holocene climate change as an important factor for human migration in West Greenland. *Proc. Natl Acad. Sci. USA* **108**, 9765–9769 (2011).
47. Calvo, E., Grimalt, J. & Jansen, E. High resolution U$^K_{37}$ sea surface temperature reconstruction in the Norwegian Sea during the Holocene. *Quat. Sci. Rev.* **21**, 1385–1394 (2002).
48. Kandiano, E. & Bauch, H. Implications of planktic foraminiferal size fractions for the glacial-interglacial paleoceanography of the polar North Atlantic. *J. Foraminifer. Res.* **32**, 245–251 (2002).
49. Werner, K., Spielhagen, R. F., Bauch, D., Hass, H. C. & Kandiano, E. Atlantic Water advection versus sea-ice advances in the eastern Fram Strait during the last 9 ka: Multiproxy evidence for a two-phase Holocene. *Paleoceanography* **28**, 283–295 (2013).
50. Werner, K. et al. Holocene sea subsurface and surface water masses in the Fram Strait–Comparisons of temperature and sea-ice reconstructions. *Quat. Sci. Rev.* **147**, 194–209 (2016).
51. England, J. H. et al. A millennial-scale record of Arctic Ocean sea ice variability and the demise of the Ellesmere Island ice shelves. *Geophys. Res. Lett.* **35**, L19502 (2008).
52. Briner, J. P. et al. Holocene climate change in Arctic Canada and Greenland. *Quat. Sci. Rev.* **147**, 340–364 (2016).
53. Oppo, D. W., McManus, J. F. & Cullen, J. L. Palaeo-oceanography: deepwater variability in the Holocene epoch. *Nature* **422**, 277–277 (2003).

54. Boyle, E. A. & Keigwin, L. North Atlantic thermohaline circulation during the past 20, 000 years linked to high-latitude surface temperature. *Nature* **330**, 35–40 (1987).

55. Kim, J.-H. et al. Impacts of the North Atlantic gyre circulation on Holocene climate off northwest Africa. *Geology* **35**, 387–390 (2007).

56. Bauch, H. A. et al. Chronology of the Holocene transgression at the North Siberian margin. *Global Planet. Change* **31**, 125–139 (2001).

57. O'Brien, S. E. Complexity of Holocene climate as reconstructed from a Greenland ice core. *Science* **270**, 1962–1964 (1995).

58. Gavin, D. G. et al. Abrupt Holocene climate change and potential response to solar forcing in western Canada. *Quat. Sci. Rev.* **30**, 1243–1255 (2011).

59. Magny, M. & Haas, J. N. A major widespread climatic change around 5300 cal. yr BP at the time of the Alpine Iceman. *J. Quat. Sci.* **19**, 423–430 (2004).

60. Nicholson, S. E. A revised picture of the structure of the "monsoon" and land ITCZ over West Africa. *Clim. Dyn.* **32**, 1155–1171 (2009).

61. Liu, Y., Chiang, J. H., Chou, C. & Patricola, C. Atmospheric teleconnection mechanisms of extratropical North Atlantic SST influence on Sahel rainfall. *Clim. Dyn.* **43**, 2797–2811 (2014).

62. Liu, Y. & Chiang, J. Coordinated abrupt weakening of the Eurasian and North African monsoons in the 1960s and links to extratropical North Atlantic cooling. *J. Clim* **25**, 3532–3548 (2012).

63. Park, J.-Y., Bader, J. Matei, D. Northern-hemispheric differential warming is the key to understanding the discrepancies in the projected Sahel rainfall. *Nat. Commun.* **6**, 5985 (2015).

64. Mulitza, S. et al. Sahel megadroughts triggered by glacial slowdowns of Atlantic meridional overturning. *Paleoceanography* **23**, PA4206 (2008).

65. Muschitiello, F., Zhang, Q., Sundqvist, H. S., Davies, F. J. & Renssen, H. Arctic climate response to the termination of the African Humid Period. *Quat. Sci. Rev.* **125**, 91–97 (2015).

66. Defrance, D. et al. Consequences of rapid ice sheet melting on the Sahelian population vulnerability. *Proc. Natl Acad. Sci. USA* **114**, 6533-6538 (2017).

67. Schulz, H. D., Devey, C. W., Pätzold, J., Fischer, G. M41/1 Cruise report. METEOR Berichte, Institut für Meereskunde der Universität Hamburg, 1–356 (1999).

68. Adegbie, A. T., Schneider, R. R., Röhl, U. & Wefer, G. Glacial millennial-scale fluctuations in central African precipitation recorded in terrigenous sediment supply and freshwater signals offshore Cameroon. *Palaeogeogr. Palaeoclimatol. Palaeoecol.* **197**, 323–333 (2003).

69. Weldeab, S., Schneider, R. R., Kölling, M. & Wefer, G. Holocene African droughts relate to eastern equatorial Atlantic cooling. *Geology* **33**, 981–984 (2005).

70. Blaauw, M. & Christen, J. Flexible paleoclimate age-depth models using an autoregressive gamma process. *Bayesian Anal.* **6**, 457–474 (2011).

71. Waelbroeck, C. et al. Sea-level and deep water temperature changes derived from benthic foraminifera isotopic records. *Quat. Sci. Rev.* **21**, 295–305 (2002).

72. Schrag, D. P. et al. The oxygen isotopic composition of seawater during the Last Glacial Maximum. *Quat. Sci. Rev.* **21**, 331–342 (2002).

73. Collins, J. A. et al. Estimating the hydrogen isotopic composition of past precipitation using leaf-waxes from western Africa. *Quat. Sci. Rev.* **65**, 88–101 (2013).

74. White, F. The vegetation of Africa. *Nat. Resour. Res.* **20**, 1 (1983).

75. Thomas, E. K. et al. Temperature and leaf wax δ^2H records demonstrate seasonal and regional controls on Asian monsoon proxies. *Geology* **42**, 1075–1078 (2014).

76. Chaudhuri, P. & Marron, J. S. SiZer for exploration of structures in curves. *J. Am. Stat. Assoc.* **94**, 807–823 (1999).

77. Collins, W. D. et al. The community climate system model version 3 (CCSM3). *J. Clim.* **19**, 2122–2143 (2006).

78. Erokhina, O. et al. Dependence of slope lapse rate over the Greenland ice sheet on background climate. *J. Glaciol.* **63**, 568–572 (2017).

79. M. Prange, S. Steph, H. Liu, L. D. Keigwin, and M. Schulz in Integrated analysis of interglacial climate dynamics (INTERDYNAMIC) (eds Schulz, M. and Paul, A.) 63–68 (Springer, Cham, 2015).

80. Roche, D. δ^{18}O water isotope in the *i*LOVECLIM model (version 1.0)–Part 1: implementation and verification. *Geosci. Model Dev.* **6**, 1481–1491 (2013).

81. Caley, T. & Roche, D. δ^{18}O water isotope in the *i*LOVECLIM model (version 1.0)–Part 2: evaluation of model results against observed δ^{18}O in water samples. *Geosci. Model Dev.* **6**, 1493–1504 (2013).

82. Caley, T. & Roche, D. δ^{18}O water isotope in the *i*LOVECLIM model (version 1.0)–Part 3: a palaeo-perspective based on present-day data–model comparison for oxygen stable isotopes in carbonates. *Geosci. Model Deve.* **6**, 1505–1516 (2013).

83. Caley, T., Roche, D. M. & Renssen, H. Orbital Asian summer monsoon dynamics revealed using an isotope-enabled global climate model. *Nat. Commun.* **5**, 5371 (2014).

84. Gimeno, L., Drumond, A., Nieto, R., Trigo, R. M. & Stohl, A. On the origin of continental precipitation. *Geophys. Res. Lett.* **37**, L13804 (2010).

85. Stohl, A., James, P. & Lagrangian, A. Analysis of the atmospheric branch of the global water cycle. Part I: method description, validation, and demonstration for the August 2002 flooding in central Europe. *J. Hydrometeorol.* **5**, 656–678 (2004).

86. Ruppert, D., Sheather, S. J. & Wand, M. P. An effective bandwidth selector for local least squares regression. *J. Am. Stat. Assoc.* **90**, 1257–1270 (1995).

87. Kim, J.-H. et al. North Pacific and North Atlantic sea-surface temperature variability during the Holocene. *Quat. Sci. Rev.* **23**, 2141–2154 (2004).

Acknowledgements

Author contributions

J.A.C. designed the study, analysed the data and wrote the manuscript. B.B. performed lipid extraction and purification, and E.S. designed the study and performed the isotopic analyses. M.P. performed the CCSM3 model analysis. T.C. and D.R. provided the *i*LOVECLIM model output. S.M. assisted with the BACON analysis. L.G. provided the FLEXPART output. All authors contributed to the discussion and interpretation.

Additional information

Supplementary Information accompanies this paper at doi:10.1038/s41467-017-01454-y.

Competing interests: The authors declare no competing financial interests.

Reprints and permission information is available online at http://npg.nature.com/reprintsandpermissions/

Publisher's note: Springer Nature remains neutral with regard to jurisdictional claims in published maps and institutional affiliations.